Environmental Science & Technology

Article

pubs.acs.org/est

Multitechnique Investigation of the pH Dependence of Phosphate Induced Transformations of ZnO Nanoparticles

Sewwandi Rathnayake,[†,‡] Jason M. Unrine,*[,†,‡] Jonathan Judy,[†,‡] Anne-Frances Miller,[§] William Rao,[†] and Paul M. Bertsch[†,‡,∥]

[†]Department of Plant and Soil Sciences, University of Kentucky, Lexington, Kentucky 40546-0312, United States

[‡]Center for Environmental Implications of Nanotechnology, Duke University, Durham, North Carolina 27708, United States

[§]Department of Chemistry, University of Kentucky, Lexington, Kentucky 40506-0055, United States

[∥]Division of Land and Water, CSIRO, Ecosciences Precinct, Brisbane, Queensland 4102, Australia

Supporting Information

ABSTRACT: In order to properly evaluate the ecological and human health risks of ZnO manufactured nanomaterials (MNMs) released to the environment, it is critical to understand the likely transformation products in various environments, such as soils, surface and ground waters, and wastewater treatment processes. To address this knowledge gap, we examined the transformation of 30 nm ZnO MNMs in the presence of different concentrations of phosphate as a function of time and pH using a variety of orthogonal analytical techniques. The data reveal that ZnO MNMs react with phosphate at various concentrations and transform into two distinct morphological/structural phases: a micrometer scale crystalline zinc phosphate phase (hopeite-like) and a nanoscale phase that likely consists of a ZnO core with an amorphous $Zn_3(PO_4)_2$ shell. The P species composition was also pH dependent, with 82% occurring as hopeite-like P at pH 6 while only 15% occurred as hopeite-like P at pH 8. These results highlight how reactions of ZnO MNMs with phosphate are influenced by environmental variables, including pH, and may ultimately result in structurally and morphologically heterogeneous end products.

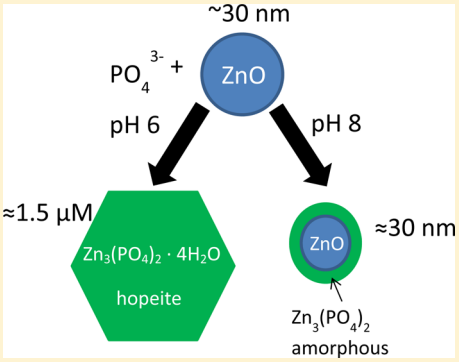

INTRODUCTION

Manufactured nanomaterials (MNMs) are increasingly being employed in consumer products such as pharmaceuticals, cosmetics, and electronics, exploiting their novel physical and chemical properties.[1,2] The commercialization of nanotechnology is expanding rapidly and is expected to be a $1 trillion (U.S. dollars) industry by 2015.[3] However, MNMs can enter the environment during their manufacturing, transport, use, and disposal and several studies have demonstrated that MNMs will be released into wastewater streams during their use from consumer items, such as textiles and personal care products.[4−6] Life-cycle inspired material flow analysis has indicated many MNMs will partition to biosolids during wastewater treatment and that soil will be a primary repository for MNMs in areas where biosolids are land applied.[2,6] Other possible routes of environmental exposure are by direct application of MNMs to agricultural fields as agrochemicals,[7,8] or direct release to surface waters from personal care products such as sunscreens[9] or as wastewater treatment effluents.[2] The potential risks to environmental and human health posed by MNMs deposited into aquatic and terrestrial ecosystems in this manner are not fully understood.

Once discharged into the environment, MNMs will be subjected to dynamic physical and chemical conditions, which will result in transformation to largely unknown end products.[10] For example, several studies have shown that silver (Ag) MNMs are readily transformed to Ag_2S during the wastewater treatment process and Ag_2S nanoparticles have been found in wastewater effluent and sludge in a pilot wastewater treatment plant,[11] as well as in field sample sewage sludge.[12] However, the structure, morphology, and mobility of Ag_2S may differ in biosolids receiving Ag^+ as compared to Ag MNMs.[13] Recently, two studies reported that ZnO MNMs rapidly transformed to ZnS and $Zn_3(PO_4)_2$ during anaerobic digestion of wastewater and post-treatment processing of sewage sludge.[14,15] These transformations are expected to dramatically alter the fundamental properties of the MNMs and will likely impact their bioavailability, toxicity, and mobility in terrestrial ecosystems. Therefore, characterizing the nature and mechansims of these transformations is essential in assessing the potential risk to the environment.[16]

Zinc oxide nanoparticles are among the highest volume MNMs used in consumer products due to their widespread use in semiconductors, pharmaceuticals, paints, personal care products, and sunscreens.[17−20] Modeling efforts predict ZnO

Received: October 10, 2013
Revised: March 18, 2014
Accepted: April 2, 2014
Published: April 2, 2014

 © 2014 American Chemical Society

MNMs will be present in wastewater treatment plant effluent in the United States at concentrations of between 0.22 to 0.74 μg L^{-1} potentially posing a toxicological risk to aquatic organisms.[17,20] Additionally, Gottschalk et al.[20] estimated that, based on usage, the concentration of ZnO MNMs in biosolids increased from 2 μg kg^{-1} to 22 μg kg^{-1} in sludge treated soil between 2005 and 2012, an increase of an order of magnitude in seven years.[20] Furthermore, ZnO MNMs are being explored for direct application to agricultural fields as a Zn amendment.[8] The bioavailability and toxicity of ZnO MNMs discharged into terrestrial ecosystems via this pathway is not well understood.

Phosphates are a major constituent of wastewater. Phosphorus input to municipal wastewater has increased since 1950 as a result of the use of laundry detergents, household cleaning products, cosmetics, and medicated shampoos.[21] A recent study revealed that the interactions between ZnO MNMs and different concentrations of phosphate resulted in the transformation of ZnO MNMs into $Zn_3(PO_4)_2$.[22] However, this study was conducted at neutral pH, but wastewater pH varies mainly between 6 and 8,[23] leaving a knowledge gap regarding the influence of pH on the final product and the transformation processes. In this study, we evaluated the transformation process at different pH values, (both acidic and alkaline conditions), over different time periods (ranging from 24 h to 7 d), and characterized the transformation products (aged MNMs) more extensively using a variety of analytical techniques. Characterization techniques included: X-ray absorption near edge structure (XANES) spectroscopy, X-ray diffraction (XRD), ^{31}P nuclear magnetic resonance (NMR) spectroscopy, and transmission electron microscopy-energy dispersive spectroscopy (TEM-EDS). The results revealed that the chemical speciation and physical form of the reaction products are dependent upon pH, phosphate concentration, and reaction time. These details should enable better prediction of the transformation of ZnO MNMs in a variety of environmental release scenarios where they are likely to encounter high phosphate concentrations at varying pH values.

■ METHODS AND MATERIALS

Dispersion and Initial Characterization of ZnO MNMs. Uncoated ZnO-Nanosun MNMs with a nominal particle diameter of 30 nm were donated by a commercial producer (Micronisers, Melbourne, Victoria, Australia). The ZnO MNMs were dispersed in the various reaction solutions at 100 mg L^{-1} concentration by continuous ultrasonication using a probe sonicator in an ice bath for 1 min (Misonix, Newtown CT, U.S.A.). This concentration was chosen to be as low as possible while allowing for sufficient material to be collected for subsequent analyses. Samples were dispersed inside 50 mL polypropylene centrifuge tubes delivering about 2150 J during each sonication treatment. Mean hydrodynamic diameters and electrophoretic mobilities of the MNM suspensions were measured using a Nano-ZS zetasizer (Malvern, Worcestershire, U.K.). Primary particle size was measured by TEM by drying the particles on 200 mesh Formvar/carbon coated Cu TEM grids (Ted Pella, Redding, CA) and the diameters of 100 randomly selected individual particles were quantified with ImageJ software (http://rsb.info.nih.gov/ij/).

Aging with Phosphate. To examine transformations over a pH range typical of wastewaters, 0, 5, 10, 50, 150 mg L^{-1} Na_2HPO_4 solutions were adjusted to pH 6 ± 0.2 or pH 8 ± 0.2 with HCl and NaOH. Then, ZnO MNMs were dispersed in the phosphate solutions at a concentration of 100 mg L^{-1} and incubated at 25 °C ± 0.1 on a shaker for 24 h, 72 h, or 7 d. Following incubation, an aliquot was removed each sample to measure the mean hydrodynamic diameter, pH, and electrophoretic mobility of the aged particles. Samples were then centrifuged at 3250*g* for 2 h to separate the solid fraction (particle size >10 nm for ZnO) from the supernatant. The separated solids were lyophilized and stored at room temperature for analysis. Supernatants were acidified to 0.15 M HNO_3 for analysis of dissolved Zn concentrations by inductively coupled plasma mass spectrometry (ICP-MS).

Dissolved Zn Analysis. Dissolved Zn^{2+} concentrations in the supernatants were quantified using an Agilent 7500cx ICP-MS (Santa Clara, CA, U.S.A.). Analytical runs contained calibration verification samples, duplicate dilutions, and spike recovery samples. Spike recovery averaged 97.7 ± 6.9% (n = 4) and the mean relative percent difference (RPD) between duplicate dilutions was 1.0 ± 2.5% (n = 4). Three replicates were prepared for all treatment combinations. Visual MINTEQ was used to predict the thermodynamic speciation and solubility of ZnO as a function of phosphate concentration and pH.

Synchrotron-Based X-ray Absorption near Edge Spectroscopy (XANES). Lyophilized powders were ground with a mortar and pestle and homogeneously distributed onto Kapton or cellophane tape for analysis by X-ray absorption near edge spectroscopy (XANES), eliminating presence of any particles larger than 1 absorption unit thickness at the Zn K-edge (47 μm). Zinc K-edge XANES spectra were collected at beamline X-26A of the National Synchrotron Light Source, Brookhaven National Laboratory (Upton, NY, U.S.A.). The beam was focused to a spot size of approximately 10 × 10 μm^2, as previously described.[24] XANES spectra were collected in transmission mode by scanning the monochromator from 9600 to 9800 eV. Layers of tape coated with samples and standards were stacked to achieve samples that were 1 ± 0.3 absorption units and to eliminate any pinholes or voids in the samples. ZnO MNM and hopeite were used as standards since hopeite was the only transformation product predicted at these pH values and solution compositions by Visual MINETEQ. The energy range was scanned as follows: 9600−9645 eV in 5 eV steps, 9645−9710 eV in 0.3 eV steps, 9710.5−9726 eV in 0.5 steps, and 9726−9800 eV in 0.5 eV steps. The XANES spectra were processed and analyzed using the Athena software package.[25] After normalization, linear combination fits (LCFs) were performed using ZnO MNM and $Zn_3(PO_4)_2$ as standards. A Zn foil was regularly used to perform energy calibration of the spectra. We verified the quality of the fits by analyzing standards containing known proportions of ZnO and $Zn_3(PO_4)_2$ performing LCFs.

X-ray Diffraction (XRD). Powder XRD analysis of aged particles performed using an X'Pert PRO MPD (PANalytical, B.V., Almelo, Netherlands) diffractometer using a Cu Kα (λ = 0.154 nm) radiation source in the 2θ scanning range of 2−60°. The XRD patterns were refined according to the high score method with the material analysis using the diffraction (v.3.0.5) software package.[26] Crystalline phases were identified by comparing experimental data with JCPDS files from the International Center for Diffraction Data (PDF files 01-071-6424 and 00-037-0465).

Solid State ^{31}P Nuclear Magnetic Resonance (NMR). Samples of 100−200 mg were packed into 5 mm zirconia NMR rotors. ^{31}P magic angle spinning (MAS) spectra were collected

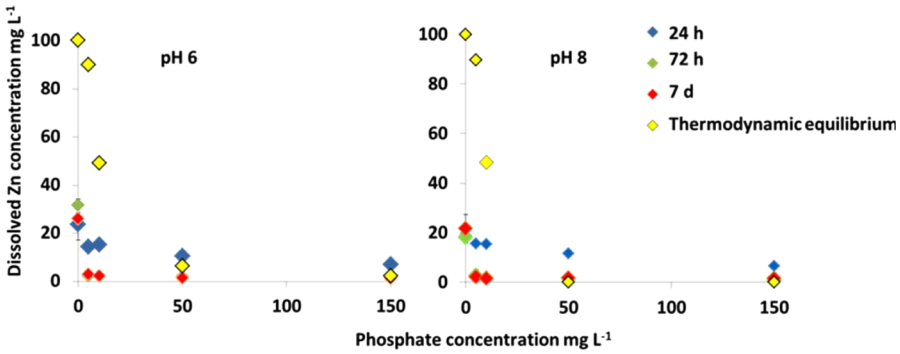

Figure 1. Concentrations of dissolved Zn^{2+} as a function of phosphate concentration, pH, and time. Each value represents the mean of three replicates with standard deviation shown by error bars.

at 162 MHz for ^{31}P (400 MHz for ^{1}H) in a 5 mm HX Chemagnetics-type probe using a Varian Inova spectrometer (Santa Clara, CA, U.S.A.). Unbiased spectra of all ^{31}P sites were collected via direct polarization (DP) of ^{31}P using a 5 μs 90° excitation pulse, 80 ms data acquisition with ^{1}H decoupling at 50 kHz,[27] and a 100 s delay between scans, unless otherwise noted. Spectra collected at MAS speeds of 3, 4, 5, and 6 kHz were used for measurement of spinning sideband intensities. These were used to calculate the principal values of the ^{31}P chemical shift tensors for each spectral component via Herzfeld-Berger analysis using the software of K. Eichele.[28,29] Averages of the principal values obtained at three different MAS speeds are reported in Table S1 (see Supporting Information, SI, Table S1). All ^{31}P chemical shifts are quoted relative to phosphoric acid (≥85% Fisher Scientific, A260−500) which was run separately, nonspinning. Spectra obtained at spinning speeds of 6 kHz were used for deconvolution of contributing signals, using Agilent's VnmrJ 3.2 software.

Spectra emphasizing ^{31}P sites near to ^{1}Hs were obtained with signal enhancement via ramped cross-polarization (CP) from ^{1}H at a CP field of 50 kHz for ^{1}H,[30] and ^{1}H TPPM2 decoupling at 50 kHz during the 80 or 50 ms acquisitions.[27] The delay between scans was 20 s. The CP contact time was varied from 0.1 to 18 ms in 12 steps to characterize polarization buildup and decay at the different ^{31}P sites due to $^{1}H-^{31}P$ cross relaxation and ^{1}H $T_{1H,\rho}$. Signal amplitudes were fit with the expression $A = M_o(1 - e^{-t/\tau cp})e^{-t/T1H,\rho}$ where τ_{cp} is the characteristic time of the buildup of ^{31}P magnetization based on CP from ^{1}H and $T_{1H,\rho}$ is the ^{1}H rotating frame longitudinal relaxation time at a CP field strength of 50 kHz (as used here).[31]

RESULTS AND DISCUSSION

Solubility of MNMs in Phosphate Solutions. Measurements of supernatants revealed that the concentrations of dissolved Zn^{2+} in the supernatants after 24 h were 23.4 mg L^{-1} and 18.8 mg L^{-1} for the pH 6 and 8 treatments, respectively (Figure 1). Concentrations of Zn^{2+} decreased both over time and with increasing phosphate concentration at both pH 6 and 8, providing evidence for transformations of the ZnO that decreased their solubility. The Zn^{2+} concentrations after 72 h and 7 d at both pH 6 and 8 were near concentrations predicted at thermodynamic equilibrium, as modeled using Visual MINTEQ, suggesting a rapid chemical transformation. The results of our modeling efforts suggest that the dissolution of ZnO MNMs results in an over saturation of Zn^{2+} with respect to a solid phase of $Zn_3(PO_4)_2.4H_2O$ (hopeite) at both pH 6 and pH 8. There was a slight increase in pH values of around 0.1−0.5 pH units between initial and final pH values irrespective of aging duration, or phosphate concentration. The one exception is at the highest phosphate concentration in the pH 8 treatment, where there was an increase of nearly 1 pH unit (SI Figure S1). This is likely due to the dissolution of ZnO, which is a proton consuming process.

XANES Data. Linear combination fit analysis of Zn K-edge XANES spectra for the solid phases formed during incubation suggest that the ZnO MNMs and phosphate reacted to form $Zn_3(PO_4)_2$ in various proportions (Figure 2, SI Figures S2 and S3). Since XANES is not sensitive to crystal structure, this could be hopeite or anhydrous $Zn_3(PO_4)_2$. The proportion of $Zn_3(PO_4)_2$ formed was a function of pH, phosphate concentration, and reaction period. Aging at pH 6 with higher phosphate concentrations for longer reaction times yielded a greater proportion of $Zn_3(PO_4)_2$ (Figure 2). At lower phosphate concentrations (5 mg L^{-1}), less than 30% of Zn is present as $Zn_3(PO_4)_2$ at both pH values. However, at 150 mg L^{-1} phosphate, more than 60% of Zn is present as $Zn_3(PO_4)_2$ at pH 6 regardless of reaction time, which is consistent with the decrease in solubility predicted by the modeling data at different phosphate concentrations. However, the pH 8 treatment had 30% or less $Zn_3(PO_4)_2$, even at 150 mg L^{-1} phosphate in the aging solution, which is less $Zn_3(PO_4)_2$ than what would be predicted at equilibrium. Linear combination fits of standards containing known proportions of ZnO and $Zn_3(PO_4)_2$ resulted in calculated proportions that were in good agreement with known proportions (SI Figure S2) and

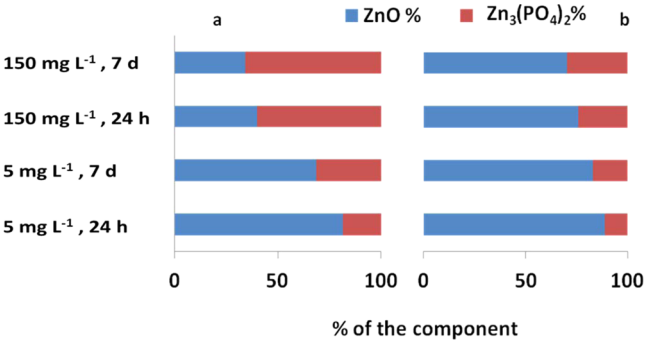

Figure 2. The quantitative distribution of aged material between ZnO and $Zn_3(PO_4)_2$ estimated from linear combination fit (LCF) analysis of X-ray near edge spectra (XANES) of manufactured ZnO nanoparticles aged in pH 6 (a) or pH 8 (b).

excellent linear combination fits were also obtained for the unknown samples with R-factors that were similar to those of the standards (SI Figure S3) .

XRD Data. XRD analysis revealed sharp, intense diffraction peaks at 2θ = 31.7, 34.4, and 36.1 in all aged MNM samples (Figure 3), which are characteristic of the presence of pristine

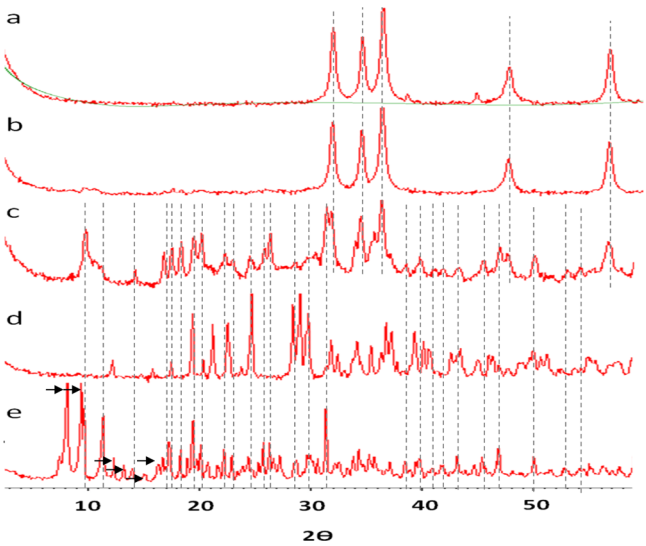

Figure 3. X-ray diffraction patterns for manufactured ZnO nanoparticles (a), particles aged at 150 mg L^{-1} phosphate for 72 h at pH 8 (b) and pH 6 (c) anhydrous $Zn_3(PO_4)_2$ (d) and hopeite (e). Dashed lines have been added to show that all peaks in the aged samples correspond to peaks in either the ZnO or hopeite standards. The black arrows indicate peaks that should not be present in the hopeite standard (see reference XRD pattern in SI) and are probably due to impurities in the reference hopeite standard.

crystalline hexagonal ZnO MNMs (pdf 01-071-6424). In addition to ZnO, at pH 6 orthorhombic hopeite is indicated by peaks at 2θ values of 9.6, 16.6, 17.3, 18.2, 19.3, 20.08, 22.18, 26.17, 31.69, and 46 (pdf 00−037−0465). Surprisingly, at pH 8 we did not observe evidence of crystalline anhydrous $Zn_3(PO_4)_2$ or hopeite in any of the XRD data (Figure 3). Since XANES can detect amorphous or crystalline phases, while XRD is only sensitive to crystalline phases, this indicates that the $Zn_3(PO_4)_2$ formed at pH 8 is amorphous.

Every recognizable peak in the pH 6 and pH 8 treatments corresponded to a peak present in either the hopeite, anhydrous $Zn_3(PO_4)_2$ or ZnO patterns. There were a few peaks present in the pattern for the hopeite standard that are not typically present in hopeite powder XRD patterns (see SI Figure S4 for a reference hopeite powder XRD pattern). This indicates that impurities were present in our commercial hopeite standard and that these peaks can be disregarded.

Surface Charge of the Aged Particles. The zeta potentials calculated from electrophoretic mobility data are shown in Figure 4. These data reveal that at both pH values, zeta potential decreases and becomes asymptotic at about −70 mV at phosphate concentrations greater than 50 mg L^{-1}. This indicates that as phosphate concentration increases, surface charge becomes increasingly negative at both pH 6 and pH 8 (Figure 4). This could be due to surface sorption of phosphate onto ZnO or due to complete transformation to $Zn_3(PO_4)_2$. The point of zero net charge for hopeite is estimated to be pH

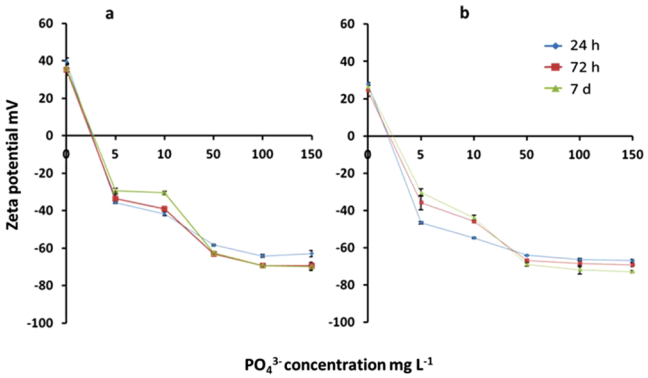

Figure 4. Zeta potential of manufactures ZnO nanoparticles aged at pH 6 (a) or pH 8 (b) as a function of phosphate concentration. Each value represents the mean of three replicates with the standard deviations shown by error bars.

4.9.[32] Such an increase in net negative surface charge may stabilize the particles in aqueous environments.

Size of the Aged Particles. TEM analysis of the unaltered ZnO MNMs used in this study revealed that individual particles were 34.2 ± 6.8 nm in diameter. The z-average (intensity weighted) diameter of the particles as measured by dynamic light scattering (DLS) in DI water was 243 ± 20 nm, indicating that at least some aggregates were present.TEM micrographs of aged particles revealed the presence of two distinct particle morphologies (Figure 5): a micro sized phase with a mean diameter of 1.4 ± 0.6 μm and a nano sized phase with a mean diameter of 29.5 ± 9.1 nm. EDS of the micro sized phase (SI Figure S5) indicated a ratio of P:Zn of 0.35 (mass basis) which is consistent with the stoichiometry of $Zn_3(PO_4)_2{\cdot}4H_2O$, where P:Zn = 0.32. The EDS data of the nanosized phase revealed a P:Zn ratio of 0.06. No P was detected in EDS spectra collected from the pristine ZnO MNMs. The mean diameter 29.5 ± 9.1 nm of the nano phase as determined from the TEM images (Figure 5) is similar in size to the pristine ZnO MNMs. Taken together, the zeta potential data, the TEM images, solubility data, the XRD data, the XANES data, and the EDS data characterizing the nano phase suggests the formation of a ZnO−$Zn_3(PO_4)_2$ core−shell structure. For example, the surface chemistry and solubility of this phase was nearly identical to $Zn_3(PO_4)_2$; however, the XRD and XANES data clearly indicate the presence of crystalline ZnO in the structure in addition to $Zn_3(PO_4)_2$. The EDS data indicate that there is not enough P present for it to be pure $Zn_3(PO_4)_2$ and neither hopeite nor anhydrous $Zn_3(PO_4)_2$ peaks appear in the XRD patterns.

NMR Data. ^{31}P Solid-State NMR (SSNMR) spectra of samples aged at pH 6 or pH 8 in 150 mg L^{-1} phosphate for 72 h are compared in Figure 6. The numbers and intensities of spinning side bands extending at 4000 Hz (24.7 ppm) intervals in both directions reflects the anisotropy of the different signals (left side of Figure 6), while the isotropic chemical shifts of the different components of each sample are distinguished in a horizontal expansion of the central region (right side of Figure 6). The spectrum of a sample of hopeite ($Zn_3(PO_4)_2{\cdot}4H_2O$) is included in both panels for comparison.

Deconvolution and simulation of the spectrum of material aged at pH 6 revealed that the material is dominated by two species: the signal at 8.0 ppm accounts for 18% of the ^{31}P in the material while the signal at 4.3 ppm accounts for 82% of the material. Material aged at pH 8 required consideration of four

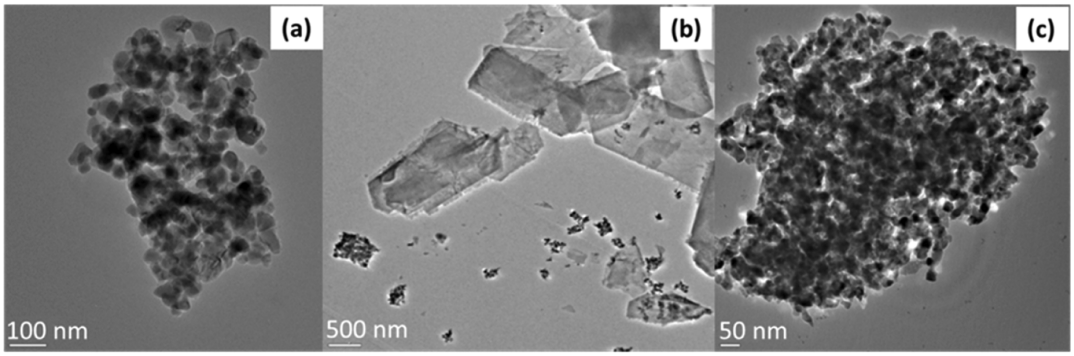

Figure 5. TEM images of pristine ZnO MNMs (a) and MNMs aged in 150 mg L^{-1} phosphate concentration for 72 h at pH 6 (b) at pH 8 (c).

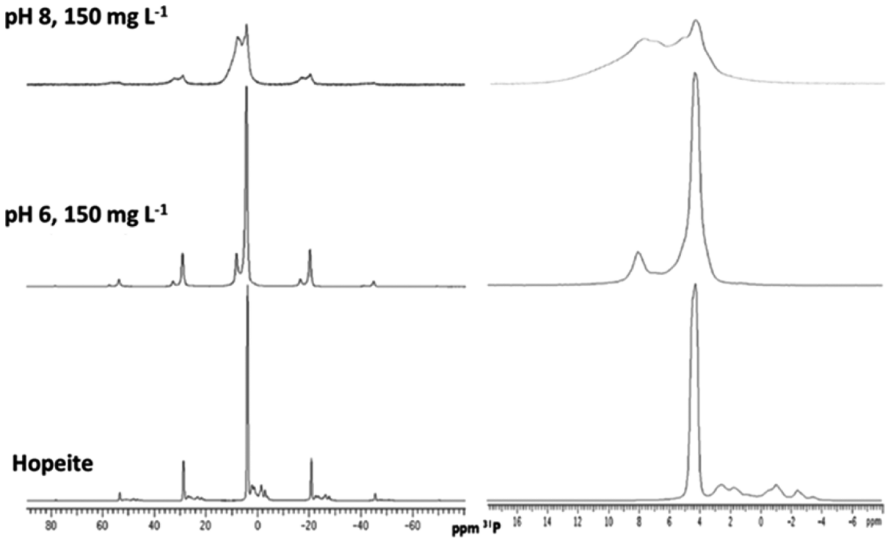

Figure 6. Comparison of ^{31}P nuclear magnetic resonance spectra of hopeite with materials aged at pH 6 vs at pH 8 in 150 mg L^{-1} phosphate. Spectra shown were obtained at a magic angle spinning speed of 4 kHz with direct polarization of ^{31}P and ^{1}H decoupling (TPPM2 at 50 kHz) during 80 ms acquisition times at room temperature with delays of 100 s between scans for hopeite and the material aged at pH 6 but 200 s for the material aged at pH 8.

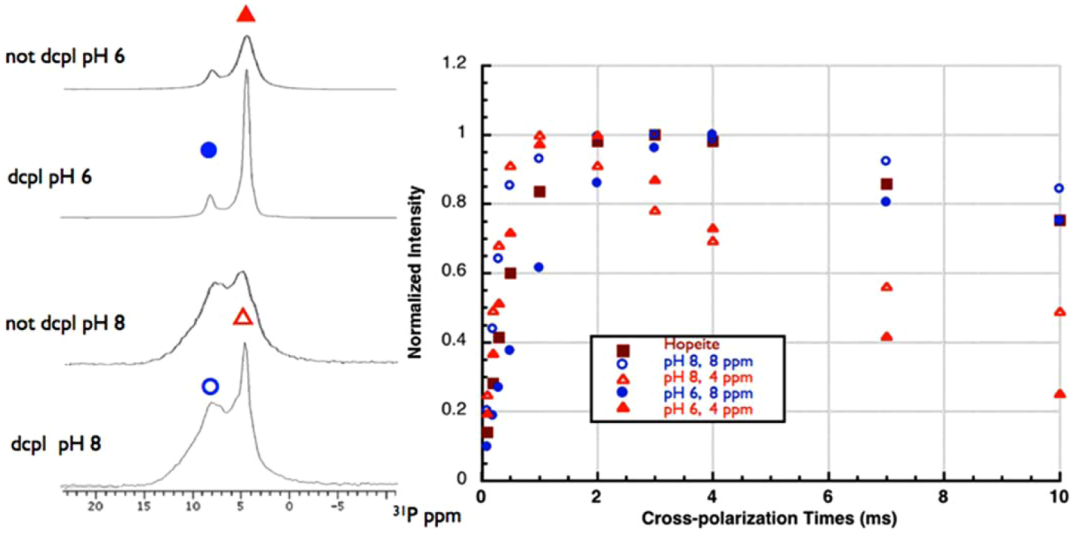

Figure 7. Effect of ^{1}H decoupling and cross-polarization on manufactured ZnO nanoparticles aged at pH 6 or pH 8. ^{31}P spectra were collected following direct polarization (left panel) or cross-polarization from ^{1}H for the time shown (right panel) prior to signal collection with ^{1}H decoupling (right panel) or decoupling as indicated (left panel). DP spectra were collected at 6 kHz MAS with 100 s delays between scans and acquisition times of 80 ms for material aged at pH 6 and hopeite, but 50 ms of data acquisition for material aged at pH 8. CP spectra were collected with 20 s delays between scans and acquisition times of 80 ms for material aged at pH 6 and 50 ms for hopeite and material aged at pH 8.

species. These are not species in the sense of mineral phases. As indicated in the XRD data, the only phase with long-range order at pH 8 is ZnO. They are different chemical environments in which P is found. Three broad components centered at 10.6, 7.9, and 5.4 ppm were obtained accounting for 10%, 4%, and 27% of the ^{31}P in the material, respectively. A sharper signal was obtained at 4.5 ppm accounting for 15% of the ^{31}P in the material. The latter is most likely due to hopeite-like sites since not only its isotropic chemical shift, but even its three principal values agreed qualitatively with those of hopeite (δ_{33} in particular proved diagnostic, see SI Table S1). It is not surprising that the three spectra do not produce signals at identical chemical shifts, since the ^{31}P signals of phosphate are responsive to pH[33] and the two aged particles were isolated from different pH values, while the pH at which the hopeite sample was isolated is not known. Thus, the NMR spectra indicate that material aged at pH 6 is 82% hopeite-like, while only 15% of the material aged at pH 8 is hopeite-like, in agreement with the XRD and XANES findings.

The dynamics of CP from ^{1}H to ^{31}P and decay of the ^{31}P signal provide additional qualitative information on the proximity of ^{1}H to the different ^{31}P sites and thus insight into the environment in which different ^{31}P species exist in the different materials. In both the pH 6 and pH 8 aged materials from 150 mg L^{-1} phosphate, the species with the chemical shift of 4.3−4.5 appears closer to more ^{1}H since this signal acquires intensity from ^{1}H faster than the signal near 8 (Figure 7, right side). The signal near 4.3−4.5 ppm is also the feature that is stronger in spectra obtained using CP than in spectra obtained using DP. This conclusion is supported by the effect of ^{1}H decoupling. Decoupling significantly sharpens the signal near 4 ppm but has a very modest effect on the signal near 8 ppm (Figure 7). Thus, we assign the signal near 4 ppm to ^{31}P nearer to more ^{1}H.

The slow decay of the hopeite signal produces better separation of the growth and decay with the result that the growth is more complete when the signal reaches maximal intensity. In contrast, for the 4.3−4.5 ppm signals from the aged MNM, decay has already had a significant impact on the signal intensity at the time we observe maximal signal intensity, so the actual full intensity is not observed, and the half-time for signal development is later than it appears. Thus, fits to the data indicate that the 4.3−4.5 ppm signal in MNM aged at pH 6 in fact has a buildup time similar to that of hopeite (SI Table S1). However, the aged MNM signal at 4.3−4.5 ppm decays more rapidly than that of hopeite under cross-polarization, in behavior that is also clearly distinct from the slower decay of the signals near 8 ppm. We speculate that this reflects a lower amount of water in the hopeite sample overall, which is relatively homogeneous. In the aged MNM, we speculate that the ^{31}P sites near ^{1}H (4 ppm) experienced enhanced relaxation due to spin diffusion from a bath of ^{1}H not directly connected to ^{31}P sites and therefore not contributing efficiently to cross-polarization. This suggests the possibility that the signal near 4 ppm represents a shell exposed to exterior water, whereas the signal near 8 ppm represents ^{31}P with less access to the proposed bath.

Environmental Implications. This study reveals that pH, phosphate concentration, and reaction time are influential in determining the final speciation, structure, and morphology of ZnO MNM transformation products. At pH 6, ZnO MNM dissolution is enhanced, with the dissolved material reprecipitating as hopeite, consistent with previous studies.[22] For ZnO MNMs aged at pH 8, XANES, and ^{31}P NMR data clearly indicate a relatively small amount of $Zn_3(PO_4)_2$ is formed compared to the pH 6 treatment. The XRD data do not indicate the presence of crystalline anhydrous $Zn_3(PO_4)_2$ or hopeite in pH 8 aged treatments, which we conclude indicates that the $Zn_3(PO_4)_2$ that forms in the pH 8 treatment is poorly ordered (amorphous). The NMR data further confirm that the phosphates in the pH 8 treatment are a mixture of four different species with a minor contribution from hopeite-like species. We speculate that after phosphatation of the surface of the pristine MNMs, the ZnO core is protected by the $Zn_3(PO_4)_2$ shell, slowing further dissolution. This suggests that although $Zn_3(PO_4)_2{\cdot}4H_2O$ is predicted at thermodynamic equilibrium at both pH values, complete transformation is kinetically limited, and limited by the formation of an insoluble shell in the pH 8 treatment.

Due to the low solubility of $Zn_3(PO_4)_2$ ($K_{sp} \approx 9 \times 10^{-33}$), dissolution of both pH 6 and pH 8 end products in the environment will be limited, limiting the potential for toxicity caused directly by released Zn^{2+}. The potential toxicity of ZnO/$Zn_3(PO_4)_2$ core−shell structures is unknown. Our previous studies and those of others did not detect ZnO in sludge from experimental wastewater treatment plants, suggesting the core−shell structure would not be present;[14,15] however, there are other potential routes of ZnO MNM introduction to the environment such as use as a fertilizer or use in sunscreens where the core−shell product may be more relevant.[8,34] Toxicity testing of these materials would be prudent given their possible occurrence in the environment under certain conditions. It is important to point out that the ZnO/$Zn_3(PO_4)_2$ core−shell structures would only likely be formed from ZnO nanoparticles and not from dissolved Zn or bulk ZnO. Further studies examining transformations of the ZnO/$Zn_3(PO_4)_2$ core−shell structures in soils, sediments, and surface water are also needed. These results highlight the complexity of potential environmental transformations of ZnO and the sensitivity of the transformation process to environmental variables. Finally, this study shows the need for a variety of approaches to probe not just the local electronic structure and coordination environment of transformation products as measured by XANES or other X-ray absorption techniques, but also their morphological and structural characteristics at the nanoscale, which could dictate subsequent environmental behavior and toxicity.

■ ASSOCIATED CONTENT

Supporting Information

The pH values at the beginning and end of aging as a function of initial pH and phosphate concentration (Figure S1); linear combination fits for X-ray absorption near edge spectra (XANES) of standards containing known proportions of ZnO and $Zn_3(PO_4)_2$ (Figure S2); example linear combination fits for X-ray absorption near edge spectra (XANES) aged ZnO manufactured nanomaterials (Figure S3); X-ray diffraction pattern for hopeite reported on the RUFF database (Figure S4); X-ray energy dispersive spectra for pristine material (A) micron-sized fraction of aged material (B) and nano-sized fraction of aged material (C) (Figure S5); additional interpretation of NMR spectra; isotropic chemical shifts (δ_{iso}) and tensors (δ_{11}, δ_{22}, and δ_{33}), T_1 relaxation times, cross-polarization buildup times (τ_{cp}) and $T_{1H,\rho}$ relaxation times for ZnO MNMs aged at pH 6 and pH 8 and standards (Table S1).

This material is available free of charge via the Internet at http://pubs.acs.org.

AUTHOR INFORMATION

Corresponding Author

*E-mail: jason.unrine@uky.edu.

Notes

The authors declare no competing financial interest.

ACKNOWLEDGMENTS

This research was supported by a grant from the U.S. Environmental Protection Agency's Science to Achieve Results (STAR) program (R834574). J.U., J.J., and P.B. were also supported by the National Science Foundation (NSF) and the Environmental Protection Agency (EPA) under NSF Cooperative Agreement EF-0830093, Center for the Environmental Implications of Nanotechnology (CEINT). Any opinions expressed in this work are those of the authors and do not necessarily reflect the official positions and policies of the USEPA. Portions of this work were performed at Beamline X26A, National Synchrotron Light Source (NSLS), and Brookhaven National Laboratory. X26A is supported by the Department of Energy (DOE)−Geosciences (DE-FG02-92ER14244 to The University of Chicago−CARS). Use of the NSLS was supported by the DOE under Contract No. DE-AC02-98CH10886. The authors gratefully acknowledge the assistance of the University of Kentucky Electron Microscopy Facility as well as T. Karathanasis, Y. Thompson, and J. Backus.

REFERENCES

(1) Tso, C.-p.; Zhung, C.-m.; Shih, Y.-h.; Tseng, Y.-M.; Wu, S.-c.; Doong, R.-a. Stability of metal oxide nanoparticles in aqueous solutions. *Water Sci. Technol.* **2010**, *61.1*, 127−133.

(2) Gottschalk, F.; Nowack, B. The release of engineered nanomaterials to the environment. *J. Environ. Monit.* **2011**, *13* (5), 1145−1155.

(3) Aitken, R. J.; Chaudhry, M. Q.; Boxall, A. B. A.; Hull, M. Manufacture and use of nanomaterials: Current status in the UK and global trends. *Occup. Med.* **2006**, *56* (5), 300−306.

(4) Miralles, P.; Church, T. L.; Harris, A. T. Toxicity, uptake, and translocation of engineered nanomaterials in vascular plants. *Environ. Sci. Technol.* **2012**, *46* (17), 9224−9239.

(5) Du, W.; Sun, Y.; Ji, R.; Zhu, J.; Wu, J.; Guo, H. TiO_2 and ZnO nanoparticles negatively affect wheat growth and soil enzyme activities in agricultural soil. *J. Environ. Monit.* **2011**, *13* (4), 822−828.

(6) Brar, S. K.; Verma, M.; Tyagi, R. D.; Surampalli, R. Y. Engineered nanoparticles in wastewater and wastewater sludge—Evidence and impacts. *Waste Manag.* **2010**, *30* (3), 504−520.

(7) Kah, M.; Hofmann, T. Nanopesticide research: Current trends and future priorities. *Environ. Int.* **2014**, *63*, 224−235.

(8) Milani, N.; McLaughlin, M. J.; Stacey, S. P.; Kirby, J. K.; Hettiarachchi, G. M.; Beak, D. G.; Cornelis, G. Dissolution kinetics of macronutrient fertilizers coated with manufactured zinc oxide nanoparticles. *J. Agric. Food Chem.* **2012**, *60* (16), 3991−3998.

(9) Botta, C.; Labille, J.; Auffan, M.; Borschneck, D.; Miche, H.; Cabié, M.; Masion, A.; Rose, J.; Bottero, J.-Y. TiO_2-based nanoparticles released in water from commercialized sunscreens in a life-cycle perspective: Structures and quantities. *Environ. Pollut.* **2011**, *159* (6), 1543−1550.

(10) Lowry, G. V.; Gregory, K. B.; Apte, S. C.; Lead, J. R. Transformations of nanomaterials in the environment. *Environ. Sci. Technol.* **2012**, *46* (13), 6893−6899.

(11) Kaegi, R.; Voegelin, A.; Sinnet, B.; Zuleeg, S.; Hagendorfer, H.; Burkhardt, M.; Siegrist, H. Behavior of metallic silver nanoparticles in a pilot wastewater treatment plant. *Environ. Sci. Technol.* **2011**, *45* (9), 3902−3908.

(12) Kim, B.; Park, C.-S.; Murayama, M.; Hochella, M. F. Discovery and characterization of silver sulfide nanoparticles in final sewage sludge products. *Environ. Sci. Technol.* **2010**, *44* (19), 7509−7514.

(13) Whitley, A. R.; Levard, C.; Oostveen, E.; Bertsch, P. M.; Matocha, C. J.; von der Kammer, F.; Unrine, J. M. Behavior of Ag nanoparticles in soil: Effects of particle surface coating, aging and sewage sludge amendment. *Environ. Pollut.* **2013**, *182*, 141−149.

(14) Lombi, E.; Donner, E.; Tavakkoli, E.; Turney, T. W.; Naidu, R.; Miller, B. W.; Scheckel, K. G. Fate of zinc oxide nanoparticles during anaerobic digestion of wastewater and post-treatment processing of sewage sludge. *Environ. Sci. Technol.* **2012**, *46* (16), 9089−9096.

(15) Ma, R.; Levard, C.; Judy, J. D.; Unrine, J. M.; Durenkamp, M.; Martin, B.; Jefferson, B.; Lowry, G. V. Fate of zinc oxide and silver nanoparticles in a pilot wastewater treatment plant and in processed biosolids. *Environ. Sci. Technol.* **2013**, *48* (1), 104−112.

(16) Scheckel, K. G.; Luxton, T. P.; El Badawy, A. M.; Impellitteri, C. A.; Tolaymat, T. M. Synchrotron speciation of silver and zinc oxide nanoparticles aged in a kaolin suspension. *Environ. Sci. Technol.* **2010**, *44* (4), 1307−1312.

(17) Reed, R. B.; Ladner, D. A.; Higgins, C. P.; Westerhoff, P.; Ranville, J. F. Solubility of nano-zinc oxide in environmentally and biologically important matrices. *Environ. Toxicol. Chem.* **2012**, *31* (1), 93−99.

(18) Rico, C. M.; Majumdar, S.; Duarte-Gardea, M.; Peralta-Videa, J. R.; Gardea-Torresdey, J. L. Interaction of nanoparticles with edible plants and their possible implications in the food chain. *J. Agric. Food Chem.* **2011**, *59* (8), 3485−3498.

(19) Lewicka, Z.; Benedetto, A.; Benoit, D.; Yu, W.; Fortner, J.; Colvin, V. The structure, composition, and dimensions of TiO_2 and ZnO nanomaterials in commercial sunscreens. *J. Nanopart. Res.* **2011**, *13* (9), 3607−3617.

(20) Gottschalk, F.; Sonderer, T.; Scholz, R. W.; Nowack, B. Modeled environmental concentrations of engineered nanomaterials (TiO_2, ZnO, Ag, CNT, fullerenes) for different regions. *Environ. Sci. Technol.* **2009**, *43* (24), 9216−9222.

(21) Litke, D. W. *Review of Phosphorus Control Measures in the United States and Their Effects on Water Quality*; US Department of the Interior, US Geological Survey: 1999.

(22) Lv, J.; Zhang, S.; Luo, L.; Han, W.; Zhang, J.; Yang, K.; Christie, P. Dissolution and microstructural transformation of ZnO nanoparticles under the influence of phosphate. *Environ. Sci. Technol.* **2012**, *46* (13), 7215−7221.

(23) Popa, P.; Timofti, M.; Voiculescu, M.; Dragan, S.; Trif, C.; Georgescu, L. P. Study of physico-chemical characteristics of wastewater in an urban agglomeration in romania. *Sci. World J.* **2012**, *2012*, 549028−549028.

(24) Unrine, J. M.; Tsyusko, O. V.; Hunyadi, S. E.; Judy, J. D.; Bertsch, P. M. Effects of particle size on chemical speciation and bioavailability of copper to earthworms (*Eisenia fetida*) exposed to copper nanoparticles. *J. Environ. Qual.* **2010**, *39* (6), 1942−1953.

(25) Ravel, B.; Newville, M. ATHENA, ARTEMIS, HEPHAESTUS: Data analysis for X-ray absorption spectroscopy using IFEFFIT. *J. Synchrotron. Radiat.* **2005**, *12* (4), 537−541.

(26) Pham, Q. N.; Bohnké, C.; Crosnier-Lopez, M.-P.; Bohnké, O. Synthesis and characterization of nanostructured fast ionic conductor $Li_{0.30}La_{0.56}TiO_3$. *Chem. Mater.* **2006**, *18* (18), 4385−4392.

(27) Bennett, A. E.; Rienstra, C. M.; Auger, M.; Lakshmi, K. V.; Griffin, R. G. Heteronuclear decouling in rotating solids. *J. Chem. Phys.* **1995**, *103* (16), 6951−6958.

(28) Herzfeld, J.; Berger, R. Sideband intensities in NMR spectra of samples spinning at the magic angle. *J. Chem. Phys.* **1980**, *73* (12), 6021−6032.

(29) Eichele, K.; Wasylishen, R. E. HBA ver. 1.5, a program for performing Herzfeld-Berger Analysis. http://anorganik.uni-tuebingen.de/klaus/soft/index.php?p=hba/hba 2005.

(30) Pines, A.; Gibby, M.; Waugh, J. Proton-enhanced NMR of dilute spins in solids. *J. Chem. Phys.* **1973**, *59* (2), 569.

(31) Lin, K. S.; Tseng, Y.-H.; Mou, Y.; Hsu, Y.-C.; Yang, C.-M.; Chan, J. C. Mechanistic study of apatite formation on bioactive glass

surface using ^{31}P solid-state NMR spectroscopy. *Chem. Mater.* **2005**, *17* (17), 4493−4501.

(32) Herschke, L.; Lieberwirth, I.; Wegner, G. Zinc phosphate as versitile material for potential biomedical applications part II. *J. Mater. Sci.: Mater. Med.* **2006**, *17*, 95−104.

(33) He, Z.; Honeycutt, C. W.; Xing, B.; McDowell, R. W.; Pellechia, P. J.; Zhang, T. Solid-state Fourier transform infrared and 31P nuclear magnetic resonance spectral features of phosphate compounds. *Soil Sci.* **2007**, *172* (7), 501−515.

(34) Auffan, M.; Chaurand, P.; Botta, C.; Labille, J.; Masion, A.; Bottero, J. Y.; Rose, J. Exposure and environmental impact during the life cycle of manufactured nanomaterials. *Acta Chim.* **2012**, No. 367, 59−62.